Generalized n-dimensional biomechanical field analysis using statistical parametric mapping

Todd C. Pataky

Department of Bioengineering, Shinshu University, Japan

Abstract

A variety of biomechanical data are sampled from smooth n-dimensional spatiotemporal fields. These data are usually analyzed discretely, by extracting summary metrics from particular points or regions in the continuum. It has been shown that, in certain situations, such schemes can compromise the spatiotemporal integrity of the original fields. An alternative methodology called Statistical Parametric Mapping (SPM), designed specifically for continuous field analysis, constructs statistical images that lie in the original, biomechanically meaningful sampling space. The current paper demonstrates how SPM can be used to analyze both experimental and simulated biomechanical field data of arbitrary spatiotemporal dimensionality. Firstly, 0-, 1-, 2-, and 3-dimensional spatiotemporal datasets derived from a pedobarographic experiment were analyzed using a common linear model to emphasize that SPM procedures are (practically) identical irrespective of the data's physical dimensionality. Secondly two probabilistic finite element simulation studies were conducted, examining heel pad stress and femoral strain fields, respectively, to demonstrate how SPM can be used to probe the significance of field-wide simulation results in the presence of uncontrollable or induced modeling uncertainty. Results were biomechanically intuitive and suggest that SPM may be suitable for a wide variety of mechanical field applications. SPM's main theoretical advantage is that it avoids problems associated with *a priori* assumptions regarding the spatiotemporal foci of field signals. SPM's main practical advantage is that a unified framework, encapsulated by a single linear equation, affords comprehensive statistical analyses of smooth scalar fields in arbitrarily bounded n-dimensional spaces.

1 Introduction

Many classes of biomechanical data share two mathematically non-trivial characteristics: (i) spatiotemporal smoothness within (ii) regular discrete bounds. This is true of 1D trajectories like vertical ground reaction forces (VGRF), and joint kinematics, 2D continua like contact pressure and surface thermal distributions, and 3D continua like bone strain and cardiac flow velocity. It is also true of simulated mechanical continua. All may be regarded as smooth scalar (or vector) fields bounded by anatomy, temporal events, or both.

These data are smooth not only because they are sampled above the Nyquist frequency, but ultimately because biological tissue viscoelasticity (Fung, 1981) causes biomechanical processes to be spatiotemporally smooth by nature. Smoothness is statistically non-trivial because it implies local data correlation and therefore that the number of independent processes is less, perhaps far less than the number of sampled points. Regular spatiotemporal bounds are also non-trivial because they imply registrability (Maintz and Viergever, 1998) and thus that a direct, continuous comparison of multiple field observations may be possible.

Since experimental and probabilistically simulated nD fields can yield a large volume of data, they are typically reduced through regionalization, by extracting multiple local VGRF optima (e.g. Nilsson and Thorstensson, 1989) or by discretizing modeled anatomy (e.g. Radcliffe and Taylor, 2007), for example. Such procedures permit statistical testing but also unfortunately create an abstraction: to understand tabular VGRF values, for example, one must mentally project these data back to their reported regions in the original sampling space. Discretization can occasionally also have statistical consequences, missing (Appendix D) or even reversing trends (Pataky et al., 2008).

A methodology called Statistical Parametric Mapping (SPM) (Friston et al., 2007) can partially offset these limitations by providing a framework for the continuous statistical analysis of smooth bounded nD fields. It was originally developed for the analysis of cerebral blood flow in 3D PET and fMRI images (Friston et al., 1991; Worsley et al., 1992) but it has since migrated to a variety of diverse applications (Worsley, 1995; Chauvin et al., 2005) including a biomechanical one (2D pedobarography) (Pataky and Goulermas, 2008). SPM's suitability for a wider range of biomechanical

applications has not yet been investigated.

The main goals of this study were to: (1) Review the mathematical foundations of nD SPM, (2) Demonstrate how SPM can be utilized for the analysis of 0-, 1-, 2-, and 3D experimental data, and (3) Demonstrate how SPM can be used in probabilistic simulations of biomechanical continua. While each demonstration is, independently, narrowly focussed it is hoped that they collectively reveal a broader utility.

2 Statistical Parametric Mapping (SPM)

2.1 General linear model (GLM)

The relation between experimental observations $\mathbf{Y}$ and an experimental design $\mathbf{X}$ can be summarized using a mass-univariate GLM (Friston et al., 1995):

$$\mathbf{Y} = \mathbf{X}\boldsymbol{\beta} + \boldsymbol{\varepsilon} \tag{1}$$

where $\boldsymbol{\beta}$ is a set of regressors (to be computed), and $\boldsymbol{\varepsilon}$ is a matrix of residuals. $\mathbf{Y}$ and $\boldsymbol{\varepsilon}$ are $(I \times K)$, $\mathbf{X}$ is appropriately scaled and $(I \times J)$, and $\boldsymbol{\beta}$ is $(J \times K)$, where I, J, and K are the numbers of observations, experimental factors, and nodes, respectively. The term 'node' is used here to refer to the number of discrete measurement points, and an experimental observation is an n-dimensional sampling of a scalar field that may be flattened into a K-vector. A full experiment yields I flattened K-vectors. Least-squares estimates of $\boldsymbol{\beta}$ can be obtained by:

$$\hat{\boldsymbol{\beta}} = \mathbf{X}^{+}\mathbf{Y} = (\mathbf{X}^{\mathrm{T}}\mathbf{X})^{-1}\mathbf{X}^{\mathrm{T}}\mathbf{Y} \tag{2}$$

yielding errors:

$$\boldsymbol{\varepsilon} = \mathbf{Y} - \mathbf{X}\hat{\boldsymbol{\beta}} \tag{3}$$

where $\mathbf{X}^{+}$ is the Moore-Penrose pseudo-inverse of $\mathbf{X}$. Like the original dataset $\mathbf{Y}$, the model fits $\mathbf{X}\hat{\boldsymbol{\beta}}$ are $(I \times K)$. In general a large proportion of variability can be explained using this approach

(see Sect.4.1).

Having estimated parameters $\hat{\boldsymbol{\beta}}$ and residuals $\boldsymbol{\varepsilon}$, the next task is to compute test statistic values. The GLM (Eqn.1) affords arbitrary linear testing including: ANOVA, ANCOVA, etc., (Friston et al., 1995), but for brevity only the generalized t test will be considered presently. First nodal variance σ_k^2 is estimated as:

$$\hat{\sigma}_k^2 = \frac{(\boldsymbol{\varepsilon}^{\mathrm{T}}\boldsymbol{\varepsilon})_{kk}}{\nu} = \frac{(\boldsymbol{\varepsilon}^{\mathrm{T}}\boldsymbol{\varepsilon})_{kk}}{I - \mathrm{rank}(\mathbf{X})} \tag{4}$$

where $(\boldsymbol{\varepsilon}^{\mathrm{T}}\boldsymbol{\varepsilon})_{kk}$ is the kth diagonal element of the $(K \times K)$ error sum of squares matrix $\boldsymbol{\varepsilon}^{\mathrm{T}}\boldsymbol{\varepsilon}$ and where ν is the error degrees of freedom. The nodal t statistic can then be computed as:

$$t_k = \frac{\mathbf{c}^{\mathrm{T}}\hat{\boldsymbol{\beta}}_k}{\hat{\sigma}_k\sqrt{\mathbf{c}^{\mathrm{T}}(\mathbf{X}^{\mathrm{T}}\mathbf{X})^{-1}\mathbf{c}}} \tag{5}$$

where $\mathbf{c}$ is a $(J \times 1)$ contrast vector. The nodal values t_k form a K-vector that can be reshaped into the original nD sampling space and viewed in the context of the original data. For this reason (5) is known as a statistical 'map' and is referred to in the literature as 'SPM{t}' (Friston et al., 2007), a notation that shall be adopted henceforth. The contrast vector $\mathbf{c}$ assigns weights to the J experimental factors and thus represents the experimental hypothesis (see Sect.3.1).

2.2 Statistical inference

SPM uses random field theory (RFT) (Adler, 1981) to assess the field-wide significance of an SPM{t}. A technical summary of RFT procedures is provided in Appendix A. Briefly, for $n>0$, RFT is charged with solving the problem of multiple comparisons. That is, one could expect to observe higher t_k values, simply by chance, when conducting multiple statistical tests. A Bonferroni correction for K multiple comparisons is valid, but is overly-conservative (in general) because spatiotemporal correlation (local smoothness) effectively ensures that fewer than K independent processes exist. RFT takes advantage of this fact to conduct inference topologically, based on the height and size of connected clusters that remain following suitably high SPM{t} thresholding (e.g. $t>3.0$). Precise probability computations additionally depend on field smoothness (Appendix B)

and search space morphology (Appendix C). A key point is that a large suprathreshold cluster is the topological equivalent of a large univariate t value. For clarity, a numerical 1D example is provided in Appendix D.

3 Methods

3.1 Experimental dataset

A single subject (male, 30 years, 172 cm, 73 kg) from a previous study (Pataky et al., 2008), verified in *post-hoc* analysis to be representative of the mean subject's statistical trends, was re-analyzed here. Since population inference was not a goal a single subject was considered appropriate. The subject performed twenty randomized repetitions of each of 'slow', 'normal', and 'fast' walking. VGRF and pedobarographic data were sampled at 500 Hz (Kistler 8281B, Winterthur, Switzerland; RSscan Footscan 3D, Olen, Belgium). Walking speed was measured at 100 Hz (ProReflex, Qualisys, Gothenburg, Sweden) and was treated as a continuous variable for statistical purposes. Prior to participation the subject gave informed consent according to the policies of the Research Ethics Committee of the University of Liverpool.

Maximal VGRF (0D), VGRF time series (1D), and peak (i.e. spatially maximal) pressure images (2D) were extracted from the original spatiotemporal (3D) pedobarographic dataset. Here the 3D data are 2D time series (and the 1D data are 0D time series), but the data were treated as mathematically 3D for volumetric smoothness, clustering, and topological probability computations (Appendix A). The 1D data were registered via linear interpolation between heel-strike and toe-off. The 2D data were registered to the chronologically first 'normal' walking image using mutual information maximization through optimal planar rigid body transformation (Pataky and Goulermas, 2008). The 3D data were registered using the optimal 2D spatial transformation followed by linear temporal interpolation, as above.

The data were modeled with four factors: main factor 'speed', an intercept, and linear and sinusoidal time drift nuisance factors (see Appendix E); the nuisance factors were included both to account for small baseline electronic drifts observed in pilot studies and to emphasize the flexibility

of the GLM for experimental modeling. The contrast vector: $\mathbf{c} = \begin{bmatrix} 1 & 0 & 0 & 0 \end{bmatrix}^{\mathrm{T}}$ (5) represents the current hypothesis: that speed is positively correlated with the outcome measure (maximal VGRF, etc.), and that the other factors are not of empirical interest. SPM analyses proceeded as described in Sect.2. All analyses were implemented in Python 2.5 using Numpy 1.3 and Scipy 0.8 as packaged with the Enthought Python Distribution 5.0 (Enthought Inc., Austin, USA).

3.2 Simulation A

An axisymmetric finite element (FE) model of heel pad indentation was constructed following (Erdemir et al., 2006) (Fig.1). The model was originally used to compute hyperelastic material properties of 20 diabetic (D) and 20 non-diabetic (ND) subjects through inverse FE simulation. Differences in the material parameters (Fig.1 caption) between the two groups failed to reach significance.

Here the reported variability is explored using Monte Carlo simulations to determine the relation between univariate material parameter significance and field-wide stress significance as assessed using SPM. Firstly, 1000 simulations were conducted for each group (D and ND) using the mean material parameters and their reported variances. Indenter depth was 8.0 mm for all simulations.

Secondly, the mean α_{D} parameter was varied between 7.0 and 7.7 in steps of 0.05 to span the range of the reported value ($\alpha_{\mathrm{D}} = 7.02$) and the univariate significance threshold ($\alpha_{\mathrm{D}} = 7.585$). For each α_{D} 1000 simulations were repeated, holding variance constant.

Finally SPM was used to compare the probabilistic Von Mises stress fields resulting from each (α_{ND},α_{D}) combination using two-sample t tests (Appendix D). Only α_{D} was varied because: (a) the implicit hypothesis of Erdemir et al. (2006) and related studies was that diabetic subjects had stiffer heel pads, and (b) this parameter affects the material's high-strain response, which is potentially of greater clinical interest than low strain. All FE problems were solved using ABAQUS 6.7 (Simulia, Providence, USA).

3.3 Simulation B

A 3D human femur model (Fig.2) was used to explore strain field changes associated with hip replacement pin placement (a simplification of Radcliffe and Taylor, 2007). Geometry was borrowed from the third-generation standardized femur model (Cheung et al., 2004). Linear material parameters (Ramos and Simões, 2006), hip contact and abductor muscle forces (Radcliffe and Taylor, 2007), and two rigid circular pin postures were modeled (see Fig.2 caption). Rather than offering orthopedic realism, this pin scheme was meant to demonstrate that SPM follows mechanical expectation.

Since hip forces are highly variable (Bergmann et al., 1993) Monte Carlo simulations were conducted (1000 repetitions for each pin configuration) by varying all force components with a standard deviation of 20% (Röhrle et al., 1984). Differences in bone strain fields between the two pin configurations were assessed using two-sample t tests (Appendix D) and irregular-lattice RFT inference procedures (Worsley et al., 1999).

4 Results

4.1 Experimental data

Experimental data (Fig.3) exhibited systematic changes with walking speed. Statistical analysis of the 0D dataset (Fig.3a) yielded t=25.1 (p=0.000), indicating significant positive correlation between walking speed and maximal VGRF. The 1D VGRF data (Figs.3b,4) were positively correlated with speed in early (0-30%) and late (75-100%) stance and were negatively correlated in mid (35-70%) stance. 2D peak pressures (Figs.3c,5) were positively correlated with walking speed at the heel and distal forefoot and negatively correlated over the distal midfoot and proximal forefoot. All effects were significant (p=0.000).

Spatiotemporal 3D pressures (Figs.3d,6) were positively correlated with walking speed under the heel, midfoot and proximal forefoot in early (0-25%) stance and under the medial forefoot and phalanges in late (75-100%) stance. Negative correlation was found throughout mid- (35-85%) stance for all areas excluding the phalanges. All three spatiotemporal clusters reached significant

(p=0.000). For reference, Table 1 lists the computed field smoothness and geometrical characteristics of all experimental datasets.

4.2 Simulation A

While mean Non-Diabetic and Diabetic heel pad stress fields exhibited differences (Figs.7a,b), SPM supported the findings of Erdemir et al. (2006) by detecting no significant field-wide effects (Fig.7c); the maximum SPM{t} (t=0.8) was unsuitably low for thresholding. However, SPM found significant broadly spanning stress responses (t >2.0, p=0.031; Fig.7d) considerably sooner (α_{D}=7.300) than univariate parameter testing (α_{D}=7.585). This increased signal sensitivity (and spatial detail evident in Fig.7d) resulted from SPM's topological treatment of the field data (Friston et al., 2007, Ch.19).

4.3 Simulation B

Mean bone strain fields were qualitatively different for the two pin configurations (Fig.8a), and SPM found these differences to be statistically significant (Fig.8b). The effects were limited to areas surrounding the pins, were maximal under the pins (the direction of the largest force component), and were biased away from the non-involved pin, as could be expected.

5 Discussion

This paper has demonstrated that SPM can be used to conduct statistical inference in a continuous and field-wide manner on nD registered biomechanical datasets. While SPM has previously been applied to 2D pedobarographic datasets (Pataky and Goulermas, 2008), the main new findings were that: (i) SPM can also be applied to smooth biomechanical field data of any physical dimensionality, and (ii) SPM can be used to probe probabilistic simulations of biomechanical continua.

5.1 Present results

The 0-2D experimental results (Figs.3-5) have been previously described elsewhere (Nilsson and Thorstensson, 1989; Rosenbaum et al., 1994; Keller et al., 1996; Taylor et al., 2004; Pataky et al.,

2008), but the 3D results (Fig.6) have not. Specifically, pressures under the midfoot and proximal forefoot appear to remain lower during slower walking throughout mid-to-late (35-85%) stance. While these results are arguably new, and although *post-hoc* analyses revealed qualitative consistency with the average subject, no population inferences are made because only a single-subject's data were presented (for clarity). The main points are that SPM appears to yield results that are biomechanically consistent with other approaches and that SPM can handle data of arbitrary dimensionality.

The present FE simulation results reveal, firstly, that SPM produces results that are consistent with mechanical expectation (Fig.8b). Secondly, SPM revealed, non-trivially, that broad continuum responses can reach statistical significance well prior to the point at which parameters governing those responses reach significance. It may therefore be prudent for future investigations to consider field-wide effects when interpreting mechanical parameter variance. These FE results collectively imply that SPM provides a suitable framework for analyses of simulated continua, and thus that it may be a useful compliment to existing probabilistic techniques (e.g. Dar et al., 2002; Laz et al., 2007).

5.2 SPM

As a field analysis method SPM has a variety of scientific merits. It is highly generalized, and thus highly flexible, and it affords both field-wide and spatiotemporally focussed hypothesis testing (Friston et al., 2007). It is mathematically very well developed and has been validated extensively (e.g. Worsley et al., 1992; Worsley, 1995). When compared with regionalization approaches, its main advantage is that it avoids two potential sources of discretization-induced bias: (i) regional conflation (Pataky et al., 2008), and (ii) *a priori* assumptions regarding spatiotemporal foci (e.g. Appendix D).

Another key advantage is that statistics are conducted on a field-wide basis, so investigators need neither devise nor adapt regionalization schemes for or to particular problems, nor would particular schemes require justification during scientific review. Along these lines, the existence of various open-source SPM packages (e.g. SPM8, Wellcome Trust Centre for Neuroimaging, University

College London) promotes a greater degree of scientific transparency than is possible with *ad hoc* or manual regionalization.

A final advantage is that statistical results lie directly in the original nD sampled continua. For example, given the context of original VGRF time series (Fig.3b), it is straightforward to interpret the corresponding SPM results (Fig.4), and one could argue that discrete extrema analysis (e.g. Fig.3a) offers a somewhat incomplete impression of the field-wide changes associated with experimental intervention.

As an aside, while SPM demands greater computational resources than regional techniques, it should be noted that analyses can still be conducted with clinically feasible speed. The current (non-compiled) Python implementation yielded statistical computation durations of: 1.48×10^{-3}, 2.95×10^{-2}, 3.31, and 14.3 s (0-3D experimental datasets, respectively); the 2- and 3D durations would likely decrease substantially via optimized compiled implementation. These durations exclude data organization coding, but a high-level automated interface could easily be constructed (e.g. click on the five pre-surgery trials, click on the five post-surgery files, GO). Registration could be performed automatically as data are collected; a recent 2D pedobarographic implementation (Oliveira et al., in press) required only $\sim$50 ms per image pair. Therefore SPM's computational demand isn't necessarily a practical limitation.

5.3 Limitations

SPM's procedures, especially those of RFT-based inference (Appendix A), are mathematically more complex than those of regional univariate (or discrete multivariate) approaches. These complexities potentially pose barriers to general adoption in investigations of biomechanical continua. However, both the availability of open-source SPM packages and the highly matured neuroimaging lead (Friston et al., 2007) could help to lower these barriers if SPM is deemed to offer empirical advantages.

From a biomechanical perspective SPM's greatest limitation is potentially its requirement for co-registration of 1D and higher dimensional datasets. One could argue, for example, that the current VGRF registration scheme yielded a misregistration of early stance peaks (Fig.3b). In

this particular case the apparent misregistration had no biomechanical consequences because the suprathreshold SPM{t} spanned broadly across early stance (Fig.4). There may be situations where SPM{t} extent is not order-of-magnitude larger than registration inaccuracy.

In such cases nonlinear registration may help (Sadeghi et al., 2003; Goulermas et al., 2005), but there are also undoubtedly situations where registration is not biomechanically feasible. Electromyographical signals with poorly defined temporal bounds or gross tissue deformity, for example, may pose practical registration problems. Qualitative geometrical manipulations of FE models (e.g. Lin et al., 2007) could also render simulation datasets unregistrable. Nevertheless, these are limitations of registration and not of SPM *per se*. Continued biomechanical registration scrutiny (Sadeghi et al., 2000; Sadeghi et al., 2003; Duhamel et al., 2004; Page and Epifanio, 2007) may help to clarify SPM's appropriateness for specific applications.

5.4 Summary

SPM affords topological statistical analysis of smooth, registrable n-dimensional scalar fields. The present results suggest that SPM may be suitable for both laboratory and probabilistic simulation studies involving a wide variety of biomechanical continua. SPM's main advantages are that statistical results lie directly in the original continuum and that potential problems associated with *ad hoc* discretization are avoided.

Acknowledgments

Funding for this work was provided by Special Coordination Funds for Promoting Science and Technology from the Japanese Ministry of Education, Culture, Sports, Science and Technology.

References

Adler, R. J. 1981. The geometry of random fields, Wiley, Chichester.

Bergmann, G., Graichen, F., and Rohlmann, A. 1993. Hip joint loading during walking and running, measured in two patients, Journal of Biomechanics 26, 969–990.

Chauvin, A., Worsley, K. J., Schyns, P. G., Arguin, M., and Gosselin, F. 2005. Accurate statistical tests for smooth classification images, Journal of Vision 5, 659–667.

Cheung, G., Zalzal, P., Bhandari, M., Spelt, J.K., and Papini, M. 2004. Finite element analysis of a femoral retrograde intramedullary nail subject to gait loading, Medical Engineering & Physics 26, 93–108.

Dar, F. H., Meakin, J. R., and Aspden, R.M. 2002. Statistical methods in finite element analysis, Journal of Biomechanics 35, 1155–1161.

Dopico-González, C., New, A. M., and Browne, M. 2009. Probabilistic finite element analysis of the uncemented hip replacement, Medical Engineering & Physics 31, 470–476.

Duhamel, A., Bourriez, J. L., Devos, P., Krystkowiak, P., Destée, A., Derambure, P., and Defebvre, L. 2004. Statistical tools for clinical gait analysis, Gait & Posture 20, 204–212.

Erdemir, A., Viveiros, M. L., Ulbrecht, J. S., and Cavanagh, P. R. 2006. An inverse finite-element model of heel-pad indentation, Journal of Biomechanics 39, 1279–1286.

Friston, K. J., Ashburner, J. T., Kiebel, S. J., Nichols, T. E., and Penny, W. D. 2007. Statistical parametric mapping: the analysis of functional brain images, Elsevier/Academic Press, Amsterdam.

Friston, K. J., Frith, C. D., Liddle, P. F., and Frackowiak, R. S. 1991. Comparing functional (PET) images: the assessment of significant change, Journal of Cerebral Blood Flow and Metabolism 11, 690–699.

Friston, K. J., Holmes, A. P., Worsley, K. J., Poline, J. P., Frith, C. D., and Frackowiak, R.S.J. 1995. Statistical parametric maps in functional imaging: a general linear approach, Human Brain Mapping 2, 189–210.

Fung, Y. C. 1981. Biomechanics: Mechanical Properties of Living Tissues., Springer-Verlag, New York.

Goulermas, J. Y., Findlow, A. H., Nester, C. J., Howard, D., and Bowker, P. 2005. Automated design of robust discriminant analysis classifier for foot pressure lesions using kinematic data, IEEE Transactions on Biomedical Engineering 52, 1549–1562.

Keller, T. S., Weisberger, A. M., Ray, J. L., Hasan, S. S., Shiavi, R. G., and Spengler, D. M. 1996. Relationship between vertical ground reaction force and speed during walking, slow jogging, and running, Clinical Biomechanics 11, 253–259.

Laz, P. J., Stowe, J. Q., Baldwin, M. A., Petrella, A. J., and Rullkoetter, P. J. 2007. Incorporating uncertainty in mechanical properties for finite element-based evaluation of bone mechanics, Journal of Biomechanics 40, 2831–2836.

Lin, C.-L., Chang, S.-H., Chang, W.-J., and Kuo, Y.-C. 2007. Factorial analysis of variables influencing mechanical characteristics of a single tooth implant placed in the maxilla using finite element analysis and the statistics-based Taguchi method, European Journal of Oral Sciences 115, 408–416.

Maintz, J. B. and Viergever, M. A. 1998. A survey of medical image registration, Medical Image Analysis 2, 1–36.

Nilsson, J. and Thorstensson, A. 1989. Ground reaction forces at different speeds of human walking and running, Acta Physiologica Scandinavica 136, 217–227.

Oliveira, F. P. M., Pataky, T. C., and Tavares, J. M. R. S. in press. Registration of pedobarographic image data in frequency domain, Computer Methods in Biomechanics and Biomedical Engineering.

Page, A. and Epifanio, I. 2007. A simple model to analyze the effectiveness of linear time normalization to reduce variability in human movement analysis, Gait & Posture 25, 153–156.

Pataky, T. C., Caravaggi, P., Savage, R., Parker, D., Goulermas, J. Y., Sellers, W. I., and Crompton, R. H. 2008. New insights into the plantar pressure correlates of walking speed using pedobarographic statistical parametric mapping (pSPM), Journal of Biomechanics 41, 1987–1994.

Pataky, T. C. and Goulermas, J. Y. 2008. Pedobarographic statistical parametric mapping (pSPM): a pixel-level approach to foot pressure image analysis, Journal of Biomechanics 41, 2136–2143.

Radcliffe, I. A. J. and Taylor, M. 2007. Investigation into the affect of cementing techniques on load transfer in the resurfaced femoral head: A multi-femur finite element analysis, Clinical Biomechanics 22, 422-430.

Ramos, A. and Simões, J. A. 2006. *Tetrahedral versus hexahedral finite elements in numerical modelling of the proximal femur*, Medical Engineering & Physics 28, 916–924.

Röhrle, H., Scholten, R., Sigolotto, C., Sollbach, W., and Kellner, H. 1984. *Joint forces in the human pelvis-leg skeleton during walking*, Journal of Biomechanics 17, 409–424.

Rosenbaum, D., Hautmann, S., Gold, M., and Claes, L. 1994. Effects of walking speed on plantar pressure patterns and hindfoot angular motion, Gait & Posture 2, 191–197.

Sadeghi, H., Allard, P., Shafie, K., Mathieu, P. A., Sadeghi, S., Prince, F., and Ramsay, J. 2000. Reduction of gait data variability using curve registration, Gait & Posture 12, 257–64.

Sadeghi, H., Mathieu, P. A., Sadeghi, S., and Labelle, H. 2003. Continuous curve registration as an intertrial gait variability reduction technique, IEEE Transactions on Neural Systems and Rehabilitation Engineering 11, 24–30.

Taylor, A. J., Menz, H. B., and Keenan, A.-M. 2004. The influence of walking speed on plantar pressure measurements using the two-step gait initiation protocol, The Foot 14, 49–55.

Worsley, K. J. 1995. Boundary corrections for the expected Euler characteristics of excursion sets of random fields, with an application to astrophysics, Advances in Applied Probability 27, 943–959.

Worsley, K. J., Andermann, M., Koulis, T., Macdonald, D., and Evans, A. C. 1999. Detecting changes in nonisotropic images, Human Brain Mapping 8, 98–101.

Worsley, K. J., Evans, A. C., Marrett, S., and Neelin, P. 1992. A three-dimensional statistical analysis for CBF activation studies in human brain, Journal of Cerebral Blood Flow and Metabolism 12, 900–918.

Table 1: Smoothness (FWHM) and geometry (resel counts R_d) of the current experimental datasets. The FWHM estimates assume isotropic and field-wide constant smoothness (see Appendix A); in the 3D case the FWHM combines spatial (5 mm) and temporal (% stance) dimensions from the current ($57 \times 23 \times 100$) (x, y, t) sampling lattice.

Dataset	FWHM	R_0	R_1	R_2	R_3
0D	-	1	-	-	-
1D	9.81	1	10.1	-	-
2D	4.34	1	19.1	33.8	-
3D	7.59	2	24.9	108.5	67.7

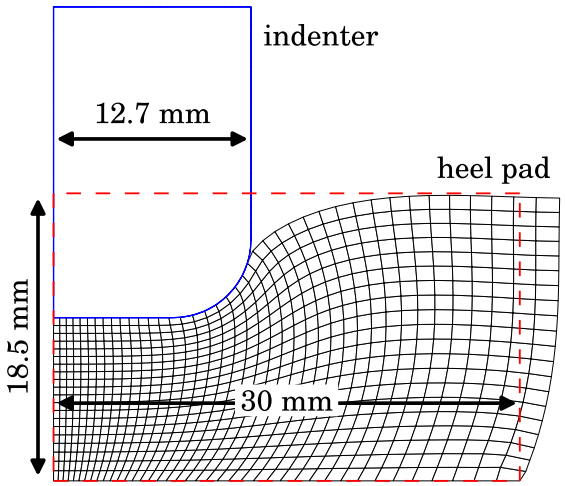

Figure 1: Axisymmetric model of heel pad indentation (adapted from Erdemir et al., 2006), 8mm indentation. The dashed rectangle depicts the undeformed geometry. The authors reported Ogden hyperelastic material parameters (means ± st.dev.) for non-diabetic (ND) and diabetic (D) groups as: μ_{ND}=16.45 (±8.27), μ_{D}=16.88 (±6.70) and α_{ND}=6.82 (±1.57), α_{D}=7.02 (±1.43), respectively.

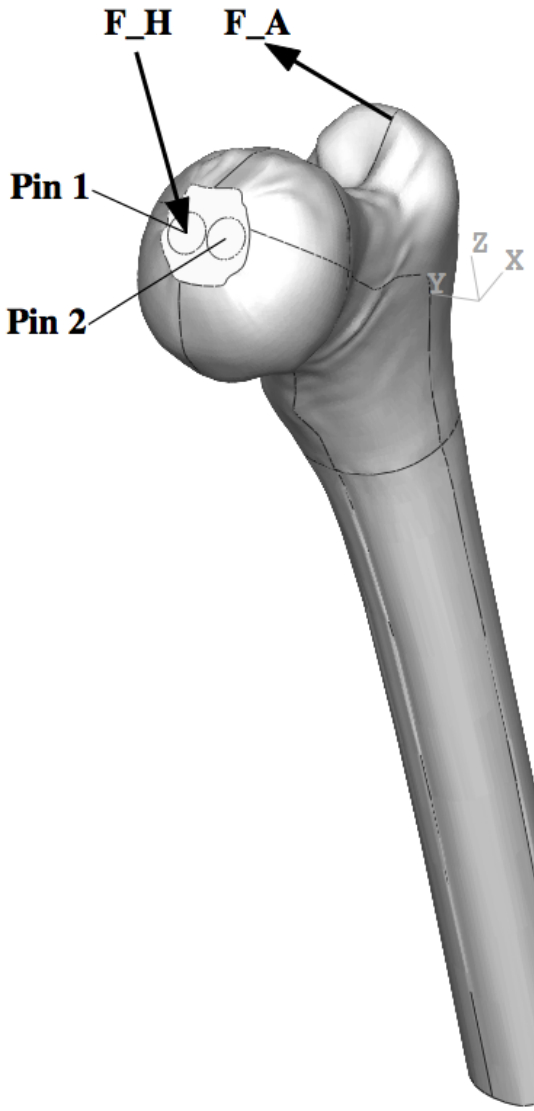

Figure 2: Three-dimensional femur model (adapted from Cheung et al., 2004). The bone was modeled as linearly elastic (E=12.8 GPa, ν=0.4) (Ramos et al., 2006). Two rigid pins were alternately placed in the depicted positions. Modeled forces (averages) included hip contact acting at the pin center ($F_H = [0.540, -0.328, -2.292]$ BW), and abductor force F_H ($F_A = [-0.580, -0.043, 1.040]$ BW) for body weight of BW=800 N (Radcliffe and Taylor, 2007). The femoral shaft was constrained from all movement at its base.

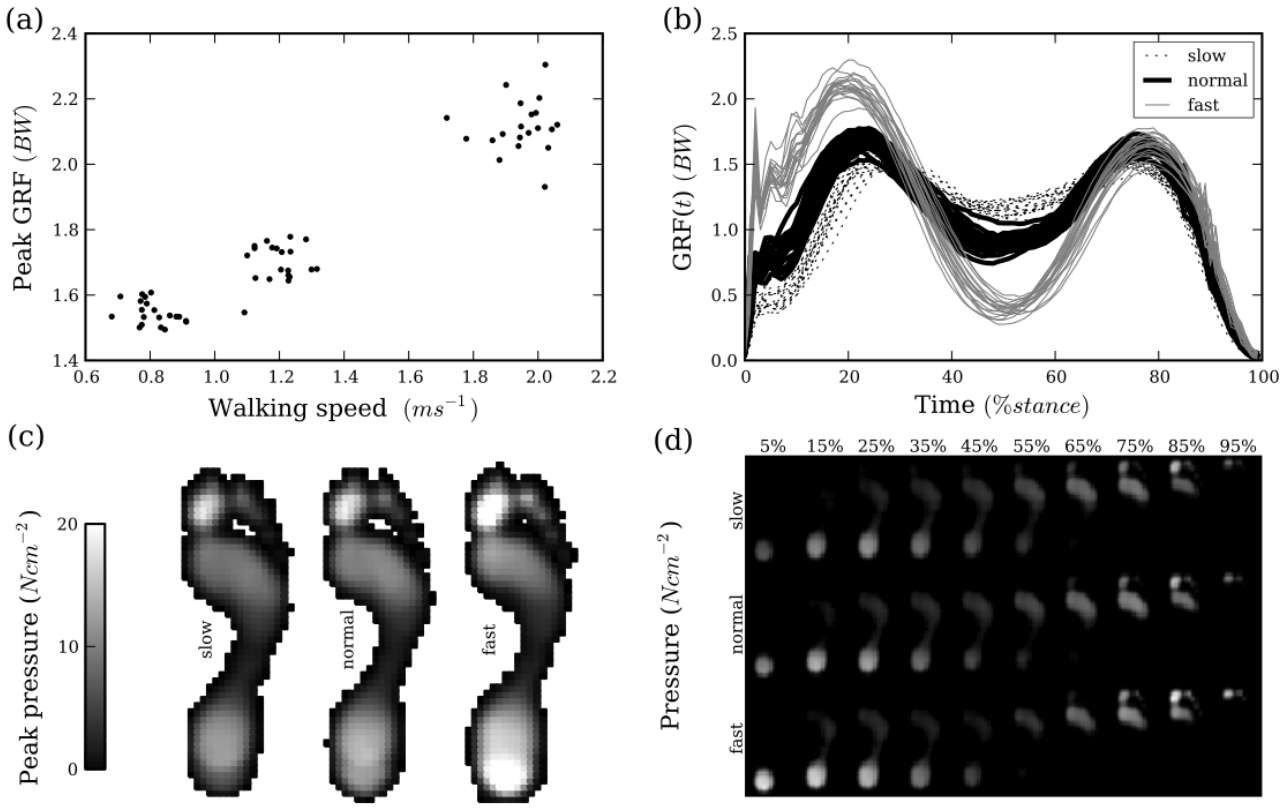

Figure 3: Experimental data. A single subject performed 20 trials of each of Slow, Normal, and Fast walking. (a) 0D raw dataset: maximal vertical ground reaction force (VGRF), normalized by body weight (BW). (b) 1D temporally registered dataset: VGRF time series. (c) 2D spatially registered dataset (means): maximal (peak) pressure. (d) 3D spatiotemporally registered dataset (means): pressure image time series.

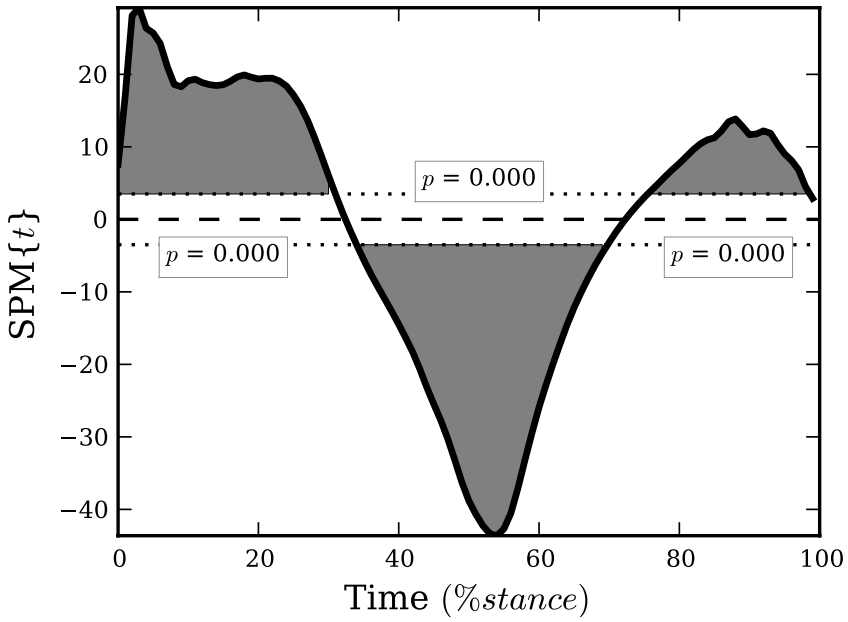

Figure 4: SPM results, 1D experimental dataset, thresholded at t >3.5. Probability (p) values indicate the likelihood that a suprathreshold cluster of the same spatiotemporal extent could have resulted from a random field process of the same smoothness as the observed residuals (Eqn.3).

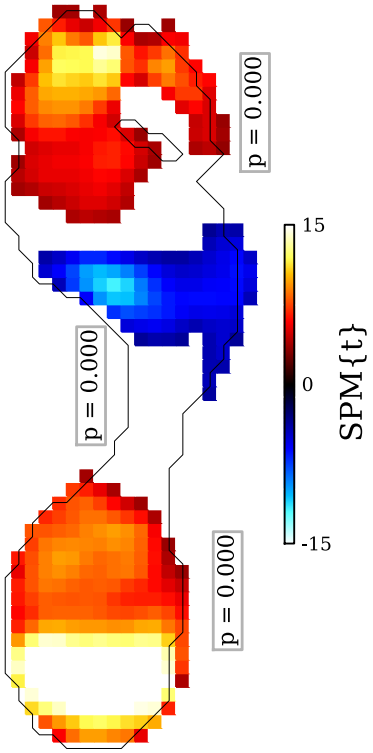

Figure 5: SPM results, 2D experimental dataset, t >3.5.

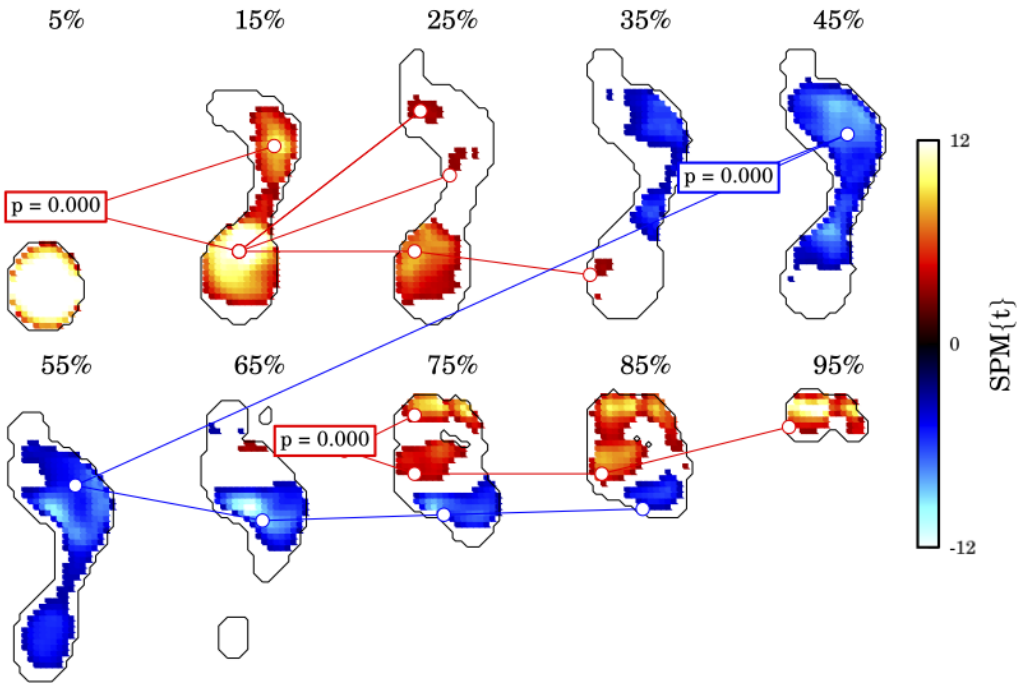

Figure 6: SPM results, 3D experimental dataset, t >3.5.

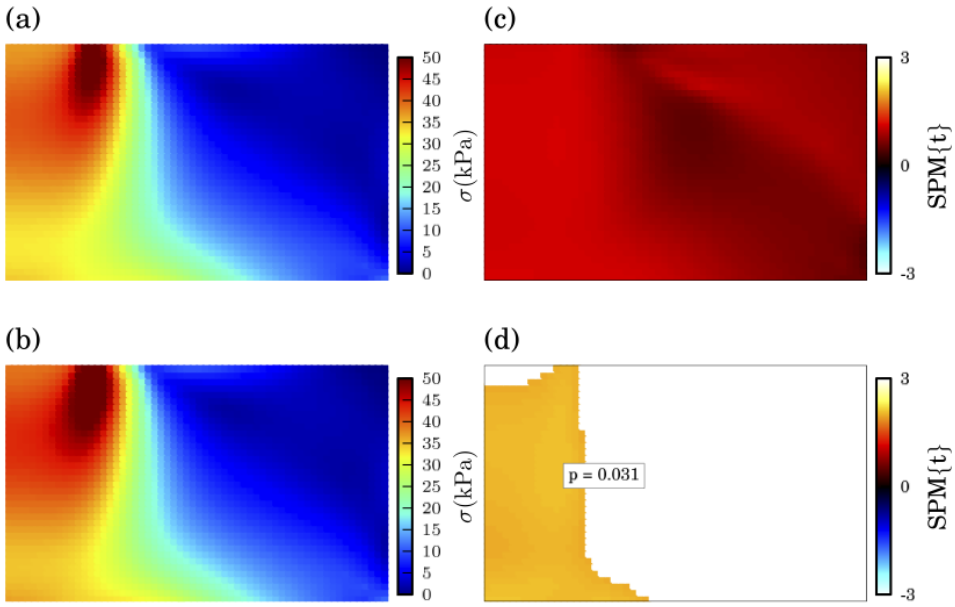

Figure 7: Heel pad simulation results, undeformed geometry. (a) Mean Non-Diabetic (ND) Von Mises (σ) field (α_{ND}=6.82). (b) Mean Diabetic (D) σ field (α_{D}=7.02). (c) SPM{t} field for mean (α_{ND}=6.82, α_{D}=7.02); SPM{t}$_{\mathrm{max}}$=0.8. (d) Inference image for α_{D}=7.300, $t > 2.0$.

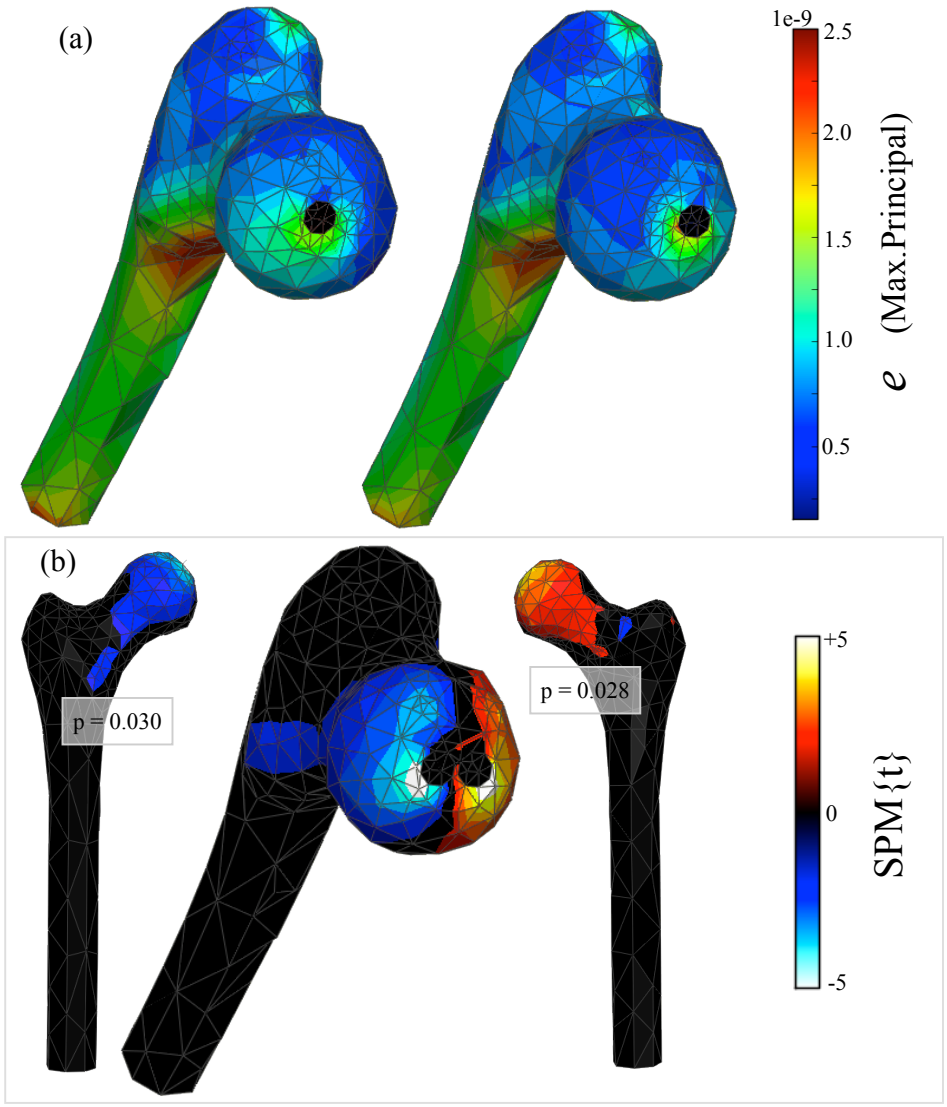

Figure 8: Femur simulation results. (a) Maximal principal strain fields for the pin1 (left) and pin2 (right) configurations under mean force vector loading. (b) SPM{t} field, (pin2-pin1), $|t| > 1.0$. Inference results for $|t| > 2.0$ are noted.

Appendix A. Statistical inference

Random field theory (RFT) (Adler, 1981) provides the mathematical foundation for conducting topological statistical inference on an SPM. Given ν, the expected topological characteristics of an SPM depend on field smoothness and search space geometry. Field smoothness can be estimated at each node by first computing normalized residuals $\mathbf{u}$ (Kiebel et al., 1999):

$$\mathbf{u}_i = \frac{\boldsymbol{\varepsilon}_i}{\sqrt{\boldsymbol{\varepsilon}_i^{\mathrm{T}} \boldsymbol{\varepsilon}_i}} \tag{A.1}$$

where i indexes the observations, then assembling an $(I \times n)$ gradient matrix at each pixel (Worsley, 2007):

$$\dot{\mathbf{u}}_k \equiv \begin{bmatrix} \boldsymbol{\nabla}(\mathbf{u}_k)_1 \\ \boldsymbol{\nabla}(\mathbf{u}_k)_2 \\ \vdots \\ \boldsymbol{\nabla}(\mathbf{u}_k)_I \end{bmatrix} = \begin{bmatrix} \frac{\partial(\mathbf{u}_k)_1}{\partial_1} & \frac{\partial(\mathbf{u}_k)_1}{\partial_2} & \cdots & \frac{\partial(\mathbf{u}_k)_1}{\partial_n} \\ \frac{\partial(\mathbf{u}_k)_2}{\partial_1} & \frac{\partial(\mathbf{u}_k)_2}{\partial_2} & \cdots & \frac{\partial(\mathbf{u}_k)_2}{\partial_n} \\ \vdots & \vdots & & \vdots \\ \frac{\partial(\mathbf{u}_k)_I}{\partial_1} & \frac{\partial(\mathbf{u}_k)_I}{\partial_2} & \cdots & \frac{\partial(\mathbf{u}_k)_I}{\partial_n} \end{bmatrix} \tag{A.2}$$

where $\boldsymbol{\nabla}(\mathbf{u}_k)_i$ is the gradient of the ith residual's kth node, and $\frac{\partial(\mathbf{u}_k)_i}{\partial_d}$ is the dth component of that gradient vector. Finally nodal smoothness can be estimated as:

$$\hat{W}_k = (4\log 2)^{\frac{1}{2}} |\dot{\mathbf{u}}_k^{\mathrm{T}} \dot{\mathbf{u}}_k|^{-\frac{1}{2n}} \tag{A.3}$$

Here $\hat{W}_k$ estimates the full-width at half-maximum (FWHM) of a Gaussian kernel that, when convolved with uncorrelated Gaussian random field data, would produce the same smoothness as was observed in the normalized residuals $\mathbf{u}_i$. As $\hat{W}_k$ increases the expected size of suprathreshold SPM{t}

clusters also increases, a fact that RFT exploits.

The expected topological characteristics of an SPM{t} also depend on the geometry of the search space $\mathbf{A}$, the nD space in which the data lie. Assuming a 3D dataset, the first step is to count the number of nodes (ρ_0), edges (ρ_d), faces ($\rho_{dd'}$), and cubes (ρ_{123}) in $\mathbf{A}$. This task can be rapidly implemented using morphological erosion (Nixon and Aguago, 2008):

$$\begin{aligned}\rho_0 &= |\mathbf{A} \ominus \mathbf{B}_0| \\ \rho_d &= |\mathbf{A} \ominus \mathbf{B}_d| \\ \rho_{dd'} &= |\mathbf{A} \ominus \mathbf{B}_{dd'}| \\ \rho_{123} &= |\mathbf{A} \ominus \mathbf{B}_{123}|\end{aligned} \tag{A.4}$$

where the $\mathbf{B}$ matrices are directional connectivity structuring elements (Appendix B). Having assembled these basic morphological characteristics of $\mathbf{A}$, its global geometry can now be summarized by 'resel' or 'resolution element' counts R_d (Worsley et al., 1996):

$$\begin{aligned}R_0 &= \rho_0 - (\rho_1 + \rho_2 + \rho_3) + (\rho_{12} + \rho_{13} + \rho_{23}) - \rho_{123} \\ R_1 &= \frac{1}{\hat{W}}\Big[(\rho_1 + \rho_2 + \rho_3) - 2(\rho_{12} + \rho_{13} + \rho_{23}) + 3\rho_{123}\Big] \\ R_2 &= \frac{1}{\hat{W}^2}\Big[(\rho_{12} + \rho_{13} + \rho_{23}) - 3\rho_{123}\Big] \\ R_3 &= \frac{1}{\hat{W}^3}[\rho_{123}]\end{aligned} \tag{A.5}$$

For simplicity A.3 assumes isotropic smoothness and A.5 assumes position-independent smoothness $\hat{W} = \Sigma\hat{W}_k/K$, but these restrictions can easily be

lifted (Worsley et al., 1999). Each R_d is associated with an independent probability density function (Worsley et al., 1996) (Appendix C) that directly depends only on the t threshold.

These density functions can be used to compute a variety of topological expectations, like the number of supra-threshold nodes and clusters, for example (Friston et al., 1994). The final steps in RFT-based inference are thus to threshold an observed SPM{t} at a suitably high value (e.g. $t > 3.0$) and then corroborate the observed topology with topological expectation, computing p values for each cluster according to Friston et al. (1994), for example. The logic of RFT is that smooth random fields are expected to produce spatially broad suprathreshold clusters, but very broad and/or very high clusters are expected to occur with low probability. The key message is that a large suprathreshold cluster is the topological equivalent of a large univariate t value.

Appendix B. Search space geometry

To rapidly compute the geometrical characteristic ρ of an nD search space defined by binary image $\mathbf{A}$, one may use morphological erosion (Nixon and Aguado, 2008):

$$\rho = |\mathbf{A} \ominus \mathbf{B}| \tag{B.1}$$

where the $\mathbf{B}$ matrices are structuring elements that describe the neighborhood connectivity of interest. In three dimensions single nodes ($\mathbf{B}_0$), adjacent nodes ($\mathbf{B}_d$), faces ($\mathbf{B}_{dd'}$), and cubes ($\mathbf{B}_{123}$) are given by the sets:

$$\begin{aligned}
\mathbf{B}_0 &= \{0,0,0\} \\
\mathbf{B}_1 &= \{\{0,0,0\},\{1,0,0\}\} \\
\mathbf{B}_2 &= \{\{0,0,0\},\{0,1,0\}\} \\
\mathbf{B}_3 &= \{\{0,0,0\},\{0,0,1\}\} \\
\mathbf{B}_{12} &= \{\{0,0,0\},\{1,0,0\},\{0,1,0\},\{1,1,0\}\} \\
\mathbf{B}_{13} &= \{\{0,0,0\},\{1,0,0\},\{0,0,1\},\{1,0,1\}\} \\
\mathbf{B}_{23} &= \{\{0,0,0\},\{0,1,0\},\{0,0,1\},\{0,1,1\}\} \\
\mathbf{B}_{123} &= \{\{0,0,0\},\{1,0,0\},\{0,1,0\},\{1,1,0\},\ldots \\
&\quad \{0,0,1\},\{1,0,1\},\{0,1,1\},\{1,1,1\}\}
\end{aligned} \tag{B.2}$$

Here $\mathbf{A} \ominus \mathbf{B}$ is an eroded binary image whose elements are ones if the $\mathbf{B}$ pattern exists at a given node and zeros otherwise. $|\mathbf{A} \ominus \mathbf{B}|$ is the set size of $\mathbf{A} \ominus \mathbf{B}$ or, equivalently, the number of ones in the eroded image.

Appendix C. Euler characteristic densities

Each 'resel count' R_d (A.5) is associated with an independent probability distribution function, or Euler characteristic density, $p_d(t)$. To three dimensions, directly from Worsley et al. (1996, Table 2), the densities are:

$$p_0(t) = \int_t^\infty \frac{\Gamma(\frac{\nu+1}{2})}{\nu\pi^{\frac{1}{2}}\Gamma(\frac{\nu}{2})}(1+\frac{u^2}{\nu})^{-\frac{1}{2}(\nu+1)}du$$

$$p_1(t) = \frac{(4\log 2)^{\frac{1}{2}}}{2\pi}\left(1+\frac{t^2}{\nu}\right)^{-\frac{1}{2}(\nu-1)}$$

$$p_2(t) = \frac{(4\log 2)}{2\pi}\frac{\Gamma(\frac{\nu+1}{2})}{(\frac{\nu}{2})^{\frac{1}{2}}\Gamma(\frac{\nu}{2})}t\left(1+\frac{t^2}{\nu}\right)^{-\frac{1}{2}(\nu-1)}$$

$$p_3(t) = \frac{(4\log 2)^{\frac{3}{2}}}{(2\pi)^2}\left(1+\frac{t^2}{\nu}\right)^{-\frac{1}{2}(\nu-1)}\left(\frac{\nu-1}{\nu}t^2-1\right)$$

where ν is the degrees of freedom. Note that p_0 is the univariate Student's t distribution. The general nD form of these distributions is given in Worsley (1994, Corollary 5.3).

Appendix D. Numerical example

Consider five fictional force trajectories from each of two experimental conditions 'A' and 'B'. (Fig.D.a) on a normalized time interval 0-100% (K=100). Condition A data were created by adding smooth Gaussian noise (FWHM=10%) to $y_{\mathrm{A}}(t)$ = 800 N. Condition B data were created by first adding positive Gaussian signals to $y_{\mathrm{B}}(t)$ = 800 N at t=75% and 15% (see Fig.D.b), and then subsequently adding filtered Gaussian noise (also at FWHM=10%). These two simulated experimental conditions were then compared using a two-sample t test (Eqn.5, main manuscript) where $\mathbf{c} = \begin{bmatrix} -1 & 1 \end{bmatrix}^{\mathrm{T}}$ and:

$$\mathbf{X} = \begin{bmatrix} 1 & 1 & 1 & 1 & 1 & 0 & 0 & 0 & 0 & 0 \\ 0 & 0 & 0 & 0 & 0 & 1 & 1 & 1 & 1 & 1 \end{bmatrix}^{\mathrm{T}} \tag{D.1}$$

After thresholding the resultant SPM{t} at $t > 3.0$, the significance of the suprathreshold clusters (Fig.D.c) was assessed using the RFT procedures described above, where the average FWHM was estimated to be 10.4% using Eqn.A.3. This simulation highlights three concepts: (i) SPM can be used to analyze continuous field data in a topological manner. (ii) A Bonferroni approach (K=100, $t_{\mathrm{critical}} = 5.192$) would fail to identify significance anywhere in the temporal field. (iii) A discrete approach that focusses only on the region t=75% would fail to identify the other signal at t=15%. While this example has been tailored to emphasize these concepts, the methodology (i) and dangers (ii,iii) clearly also apply to real experimental data.

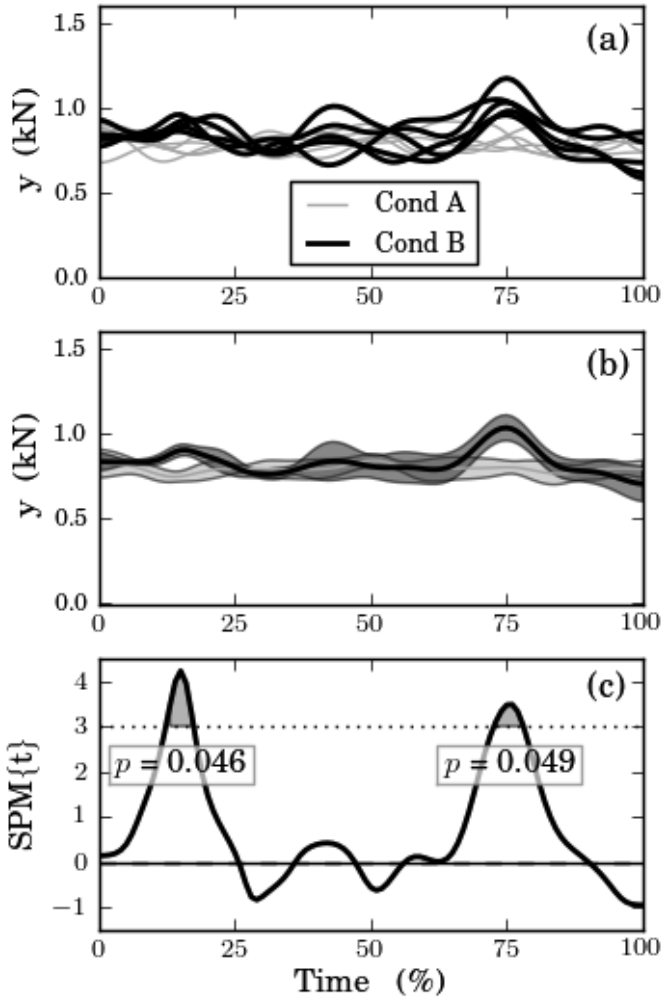

Figure D: Example 1D SPM analysis. (a) Simulated raw data for two experimental conditions 'A' and 'B'. (b) Mean curves with standard deviation clouds. (c) SPM{t} with threshold t>3.0. The p values were computed according to Appendix A-C and indicate the probability that the specific suprathreshold cluster could have occurred by chance.

Appendix E. Model visualization

The general linear model (GLM) (Eqn.1, main manuscript) consists of: experimental observations ($\mathbf{Y}$), experimental design ($\mathbf{X}$), regression coefficients ($\boldsymbol{\beta}$), and model errors ($\boldsymbol{\varepsilon}$). Since these matrices can be quite large, numerical probing of their elements is inconvenient. The elements may, however, be conveniently probed qualitatively using matrix visualization techniques. The most important matrix to visualize is $\mathbf{X}$ because it represents the experimenter's statistical modeling decisions: it describes all modeled experimental factors, it reveals the randomness of the design, and together with a contrast vector (Eqn.5, main manuscript) it explicitly describes the experimental hypothesis.

Fig.E.1 depicts the design matrix that was used to analyze the current pedobarographic data. Rows correspond to trials, and columns to modeled experimental factors. The main factor of interest was 'speed', and the first column of Fig.E.1 reveals that walking speeds were randomized. Three factors of non-interest were also also modeled: an intercept 'y_0' and two low-frequency time-drift nuisance factors. Visualizing these factors as a matrix image can be helpful to understand the experimental design, so $\mathbf{X}$ renderings like Fig.E.1 are often presented in scientific papers.

It is also instructive to visualize the entire GLM (Fig.E.2). The observations $\mathbf{Y}$ may be regarded as a bird's eye view of Fig.3a. The model fits ($\mathbf{X}\hat{\boldsymbol{\beta}}$) closely resemble the experimental data ($\mathbf{Y}$), with only relatively minor differences (ε). This indicates, anecdotally, that the GLM can explain a large proportion of the experimental variability.

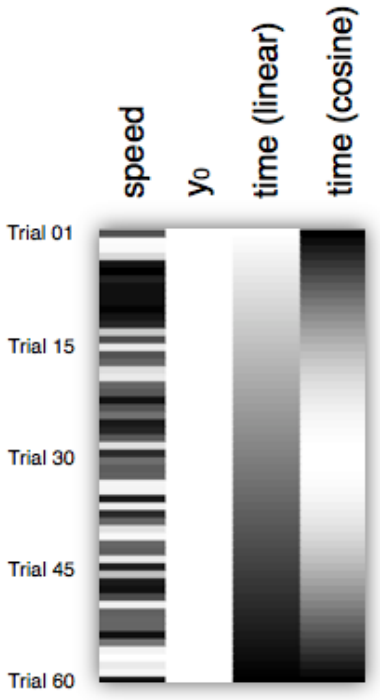

Figure E.1: Design matrix $\mathbf{X}$ (Eqn.1, main manuscript). The matrix is (60×4): 60 trials and 4 modeled experimental factors. The color scale is normalized within columns.

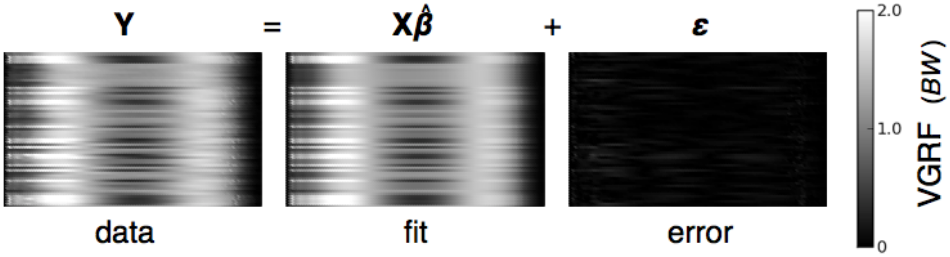

Figure E.2: Grayscale renderings of the general linear model matrices (Eqn.1, main manuscript) for the 1D VGRF dataset. Each matrix is (60×100): 60 trials and 100 VGRF trajectory nodes per trial. Absolute errors $|\varepsilon|$ are presented.

References

Adler, R. J. 1981. The geometry of random fields, Wiley, Chichester.

Friston, K. J., Worsley, K. J., Frackowiak, R. S. J., Mazziotta, J. C., and Evans, A. C. 1994. Assessing the significance of focal activations using their spatial extent, Human Brain Mapping 1, 210–220.

Kiebel, S. J., Poline, J. B., Friston, K. J., Holmes, A. P., and Worsley, K. J. 1999. Robust smoothness estimation in statistical parametric maps using standardized residuals from the general linear model, Neuroimage 10, 756–766.

Nixon, M. and Aguado, A. 2008. Feature extraction & image processing, second edition, 2nd ed., Academic Press.

Worsley, K. J. 1994. Local maxima and the expected Euler characteristic of excursion sets of χ^2, F and t fields, Advances in Applied Probability 26, 13–42.

Worsley, K. J. 2007. Random field theory. In: Statistical parametric mapping: the analysis of functional brain images (K.J. et al. Friston, ed.), Elsevier/Academic Press, Amsterdam.

Worsley, K. J., Andermann, M., Koulis, T., Macdonald, D., and Evans, A. C. 1999. Detecting changes in nonisotropic images, Human Brain Mapping 8, 98–101.

Worsley, K. J., Marrett, S., Neelin, P., Vandal, A. C., Friston, K. J., and Evans, A. C. 1996. A unified statistical approach for determining significant signals in images of cerebral activation, Human Brain Mapping 4, 58–73.

Appendix A. Statistical inference

Random field theory (RFT) (Adler, 1981) provides the mathematical foundation for conducting topological statistical inference on an SPM. Given ν, the expected topological characteristics of an SPM depend on field smoothness and search space geometry. Field smoothness can be estimated at each node by first computing normalized residuals $\mathbf{u}$ (Kiebel et al., 1999):

$$\mathbf{u}_i = \frac{\boldsymbol{\varepsilon}_i}{\sqrt{\boldsymbol{\varepsilon}_i^{\mathrm{T}} \boldsymbol{\varepsilon}_i}} \tag{A.1}$$

where i indexes the observations, then assembling an $(I \times n)$ gradient matrix at each pixel (Worsley, 2007):

$$\dot{\mathbf{u}}_k \equiv \begin{bmatrix} \boldsymbol{\nabla}(\mathbf{u}_k)_1 \\ \boldsymbol{\nabla}(\mathbf{u}_k)_2 \\ \vdots \\ \boldsymbol{\nabla}(\mathbf{u}_k)_I \end{bmatrix} = \begin{bmatrix} \frac{\partial(\mathbf{u}_k)_1}{\partial_1} & \frac{\partial(\mathbf{u}_k)_1}{\partial_2} & \cdots & \frac{\partial(\mathbf{u}_k)_1}{\partial_n} \\ \frac{\partial(\mathbf{u}_k)_2}{\partial_1} & \frac{\partial(\mathbf{u}_k)_2}{\partial_2} & \cdots & \frac{\partial(\mathbf{u}_k)_2}{\partial_n} \\ \vdots & \vdots & & \vdots \\ \frac{\partial(\mathbf{u}_k)_I}{\partial_1} & \frac{\partial(\mathbf{u}_k)_I}{\partial_2} & \cdots & \frac{\partial(\mathbf{u}_k)_I}{\partial_n} \end{bmatrix} \tag{A.2}$$

where $\boldsymbol{\nabla}(\mathbf{u}_k)_i$ is the gradient of the ith residual's kth node, and $\frac{\partial(\mathbf{u}_k)_i}{\partial_d}$ is the dth component of that gradient vector. Finally nodal smoothness can be estimated as:

$$\hat{W}_k = (4\log 2)^{\frac{1}{2}} |\dot{\mathbf{u}}_k^{\mathrm{T}} \dot{\mathbf{u}}_k|^{-\frac{1}{2n}} \tag{A.3}$$

Here $\hat{W}_k$ estimates the full-width at half-maximum (FWHM) of a Gaussian kernel that, when convolved with uncorrelated Gaussian random field data, would produce the same smoothness as was observed in the normalized residuals $\mathbf{u}_i$. As $\hat{W}_k$ increases the expected size of suprathreshold SPM{t}

clusters also increases, a fact that RFT exploits.

The expected topological characteristics of an SPM{t} also depend on the geometry of the search space $\mathbf{A}$, the nD space in which the data lie. Assuming a 3D dataset, the first step is to count the number of nodes (ρ_0), edges (ρ_d), faces ($\rho_{dd'}$), and cubes (ρ_{123}) in $\mathbf{A}$. This task can be rapidly implemented using morphological erosion (Nixon and Aguago, 2008):

$$\begin{aligned}\rho_0 &= |\mathbf{A} \ominus \mathbf{B}_0| \\ \rho_d &= |\mathbf{A} \ominus \mathbf{B}_d| \\ \rho_{dd'} &= |\mathbf{A} \ominus \mathbf{B}_{dd'}| \\ \rho_{123} &= |\mathbf{A} \ominus \mathbf{B}_{123}|\end{aligned} \tag{A.4}$$

where the $\mathbf{B}$ matrices are directional connectivity structuring elements (Appendix B). Having assembled these basic morphological characteristics of $\mathbf{A}$, its global geometry can now be summarized by 'resel' or 'resolution element' counts R_d (Worsley et al., 1996):

$$\begin{aligned}R_0 &= \rho_0 - (\rho_1 + \rho_2 + \rho_3) + (\rho_{12} + \rho_{13} + \rho_{23}) - \rho_{123} \\ R_1 &= \frac{1}{\hat{W}}\Big[(\rho_1 + \rho_2 + \rho_3) - 2(\rho_{12} + \rho_{13} + \rho_{23}) + 3\rho_{123}\Big] \\ R_2 &= \frac{1}{\hat{W}^2}\Big[(\rho_{12} + \rho_{13} + \rho_{23}) - 3\rho_{123}\Big] \\ R_3 &= \frac{1}{\hat{W}^3}[\rho_{123}]\end{aligned} \tag{A.5}$$

For simplicity A.3 assumes isotropic smoothness and A.5 assumes position-independent smoothness $\hat{W} = \Sigma\hat{W}_k/K$, but these restrictions can easily be

lifted (Worsley et al., 1999). Each R_d is associated with an independent probability density function (Worsley et al., 1996) (Appendix C) that directly depends only on the t threshold.

These density functions can be used to compute a variety of topological expectations, like the number of supra-threshold nodes and clusters, for example (Friston et al., 1994). The final steps in RFT-based inference are thus to threshold an observed SPM{t} at a suitably high value (e.g. $t > 3.0$) and then corroborate the observed topology with topological expectation, computing p values for each cluster according to Friston et al. (1994), for example. The logic of RFT is that smooth random fields are expected to produce spatially broad suprathreshold clusters, but very broad and/or very high clusters are expected to occur with low probability. The key message is that a large suprathreshold cluster is the topological equivalent of a large univariate t value.

Appendix B. Search space geometry

To rapidly compute the geometrical characteristic ρ of an nD search space defined by binary image $\mathbf{A}$, one may use morphological erosion (Nixon and Aguado, 2008):

$$\rho = |\mathbf{A} \ominus \mathbf{B}| \tag{B.1}$$

where the $\mathbf{B}$ matrices are structuring elements that describe the neighborhood connectivity of interest. In three dimensions single nodes ($\mathbf{B}_0$), adjacent nodes ($\mathbf{B}_d$), faces ($\mathbf{B}_{dd'}$), and cubes ($\mathbf{B}_{123}$) are given by the sets:

$$\begin{aligned}
\mathbf{B}_0 &= \{0,0,0\} \\
\mathbf{B}_1 &= \{\{0,0,0\},\{1,0,0\}\} \\
\mathbf{B}_2 &= \{\{0,0,0\},\{0,1,0\}\} \\
\mathbf{B}_3 &= \{\{0,0,0\},\{0,0,1\}\} \\
\mathbf{B}_{12} &= \{\{0,0,0\},\{1,0,0\},\{0,1,0\},\{1,1,0\}\} \\
\mathbf{B}_{13} &= \{\{0,0,0\},\{1,0,0\},\{0,0,1\},\{1,0,1\}\} \\
\mathbf{B}_{23} &= \{\{0,0,0\},\{0,1,0\},\{0,0,1\},\{0,1,1\}\} \\
\mathbf{B}_{123} &= \{\{0,0,0\},\{1,0,0\},\{0,1,0\},\{1,1,0\},\ldots \\
&\quad \{0,0,1\},\{1,0,1\},\{0,1,1\},\{1,1,1\}\}
\end{aligned} \tag{B.2}$$

Here $\mathbf{A} \ominus \mathbf{B}$ is an eroded binary image whose elements are ones if the $\mathbf{B}$ pattern exists at a given node and zeros otherwise. $|\mathbf{A} \ominus \mathbf{B}|$ is the set size of $\mathbf{A} \ominus \mathbf{B}$ or, equivalently, the number of ones in the eroded image.

Appendix C. Euler characteristic densities

Each 'resel count' R_d (A.5) is associated with an independent probability distribution function, or Euler characteristic density, $p_d(t)$. To three dimensions, directly from Worsley et al. (1996, Table 2), the densities are:

$$p_0(t) = \int_t^\infty \frac{\Gamma(\frac{\nu+1}{2})}{\nu\pi^{\frac{1}{2}}\Gamma(\frac{\nu}{2})}(1+\frac{u^2}{\nu})^{-\frac{1}{2}(\nu+1)}du$$

$$p_1(t) = \frac{(4\log 2)^{\frac{1}{2}}}{2\pi}\left(1+\frac{t^2}{\nu}\right)^{-\frac{1}{2}(\nu-1)}$$

$$p_2(t) = \frac{(4\log 2)}{2\pi}\frac{\Gamma(\frac{\nu+1}{2})}{(\frac{\nu}{2})^{\frac{1}{2}}\Gamma(\frac{\nu}{2})}t\left(1+\frac{t^2}{\nu}\right)^{-\frac{1}{2}(\nu-1)}$$

$$p_3(t) = \frac{(4\log 2)^{\frac{3}{2}}}{(2\pi)^2}\left(1+\frac{t^2}{\nu}\right)^{-\frac{1}{2}(\nu-1)}\left(\frac{\nu-1}{\nu}t^2-1\right)$$

where ν is the degrees of freedom. Note that p_0 is the univariate Student's t distribution. The general nD form of these distributions is given in Worsley (1994, Corollary 5.3).

Appendix D. Numerical example

Consider five fictional force trajectories from each of two experimental conditions 'A' and 'B'. (Fig.D.a) on a normalized time interval 0-100% (K=100). Condition A data were created by adding smooth Gaussian noise (FWHM=10%) to $y_{\mathrm{A}}(t)$ = 800 N. Condition B data were created by first adding positive Gaussian signals to $y_{\mathrm{B}}(t)$ = 800 N at t=75% and 15% (see Fig.D.b), and then subsequently adding filtered Gaussian noise (also at FWHM=10%). These two simulated experimental conditions were then compared using a two-sample t test (Eqn.5, main manuscript) where $\mathbf{c} = \begin{bmatrix} -1 & 1 \end{bmatrix}^{\mathrm{T}}$ and:

$$\mathbf{X} = \begin{bmatrix} 1 & 1 & 1 & 1 & 1 & 0 & 0 & 0 & 0 & 0 \\ 0 & 0 & 0 & 0 & 0 & 1 & 1 & 1 & 1 & 1 \end{bmatrix}^{\mathrm{T}} \tag{D.1}$$

After thresholding the resultant SPM{t} at $t > 3.0$, the significance of the suprathreshold clusters (Fig.D.c) was assessed using the RFT procedures described above, where the average FWHM was estimated to be 10.4% using Eqn.A.3. This simulation highlights three concepts: (i) SPM can be used to analyze continuous field data in a topological manner. (ii) A Bonferroni approach (K=100, $t_{\mathrm{critical}} = 5.192$) would fail to identify significance anywhere in the temporal field. (iii) A discrete approach that focusses only on the region t=75% would fail to identify the other signal at t=15%. While this example has been tailored to emphasize these concepts, the methodology (i) and dangers (ii,iii) clearly also apply to real experimental data.

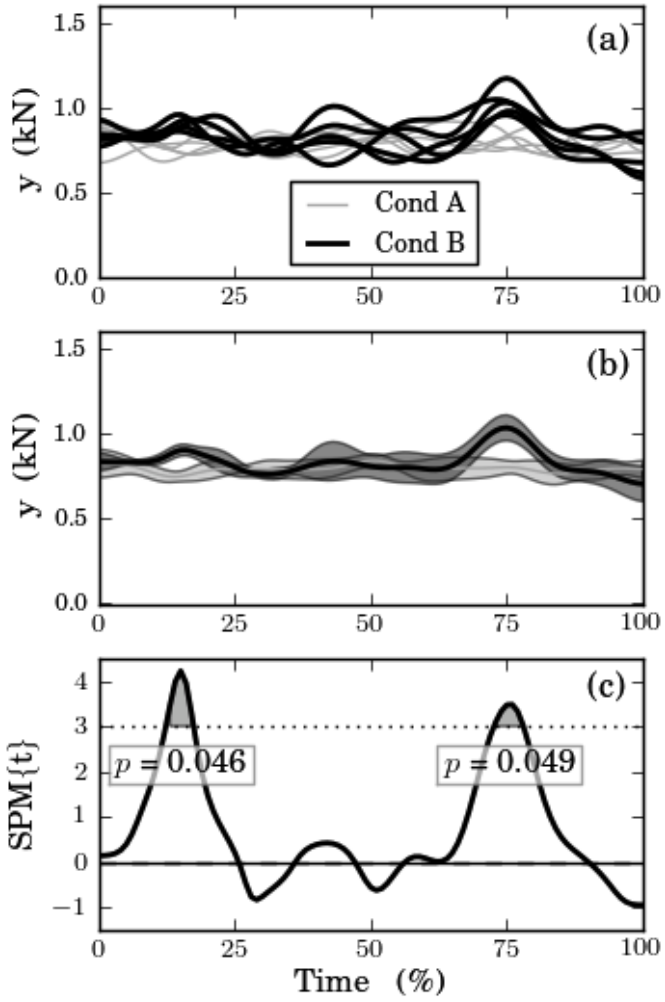

Figure D: Example 1D SPM analysis. (a) Simulated raw data for two experimental conditions 'A' and 'B'. (b) Mean curves with standard deviation clouds. (c) SPM{t} with threshold t>3.0. The p values were computed according to Appendix A-C and indicate the probability that the specific suprathreshold cluster could have occurred by chance.

Appendix E. Model visualization

The general linear model (GLM) (Eqn.1, main manuscript) consists of: experimental observations ($\mathbf{Y}$), experimental design ($\mathbf{X}$), regression coefficients ($\boldsymbol{\beta}$), and model errors ($\boldsymbol{\varepsilon}$). Since these matrices can be quite large, numerical probing of their elements is inconvenient. The elements may, however, be conveniently probed qualitatively using matrix visualization techniques. The most important matrix to visualize is $\mathbf{X}$ because it represents the experimenter's statistical modeling decisions: it describes all modeled experimental factors, it reveals the randomness of the design, and together with a contrast vector (Eqn.5, main manuscript) it explicitly describes the experimental hypothesis.

Fig.E.1 depicts the design matrix that was used to analyze the current pedobarographic data. Rows correspond to trials, and columns to modeled experimental factors. The main factor of interest was 'speed', and the first column of Fig.E.1 reveals that walking speeds were randomized. Three factors of non-interest were also also modeled: an intercept 'y_0' and two low-frequency time-drift nuisance factors. Visualizing these factors as a matrix image can be helpful to understand the experimental design, so $\mathbf{X}$ renderings like Fig.E.1 are often presented in scientific papers.

It is also instructive to visualize the entire GLM (Fig.E.2). The observations $\mathbf{Y}$ may be regarded as a bird's eye view of Fig.3a. The model fits ($\mathbf{X}\hat{\boldsymbol{\beta}}$) closely resemble the experimental data ($\mathbf{Y}$), with only relatively minor differences (ε). This indicates, anecdotally, that the GLM can explain a large proportion of the experimental variability.

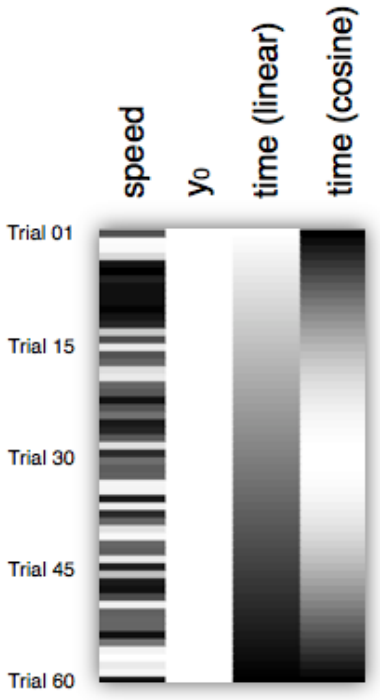

Figure E.1: Design matrix $\mathbf{X}$ (Eqn.1, main manuscript). The matrix is (60×4): 60 trials and 4 modeled experimental factors. The color scale is normalized within columns.

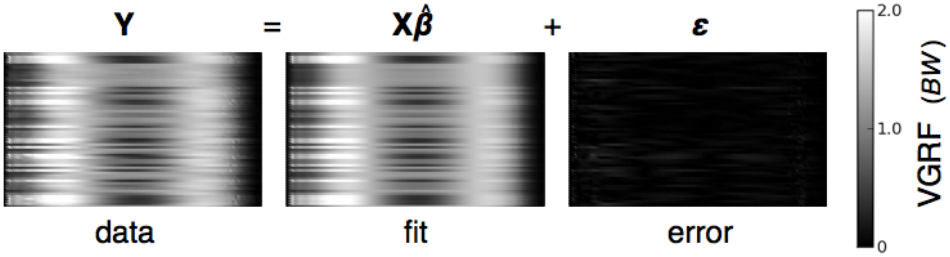

Figure E.2: Grayscale renderings of the general linear model matrices (Eqn.1, main manuscript) for the 1D VGRF dataset. Each matrix is (60×100): 60 trials and 100 VGRF trajectory nodes per trial. Absolute errors $|\varepsilon|$ are presented.

References

Adler, R. J. 1981. The geometry of random fields, Wiley, Chichester.

Friston, K. J., Worsley, K. J., Frackowiak, R. S. J., Mazziotta, J. C., and Evans, A. C. 1994. Assessing the significance of focal activations using their spatial extent, Human Brain Mapping 1, 210–220.

Kiebel, S. J., Poline, J. B., Friston, K. J., Holmes, A. P., and Worsley, K. J. 1999. Robust smoothness estimation in statistical parametric maps using standardized residuals from the general linear model, Neuroimage 10, 756–766.

Nixon, M. and Aguado, A. 2008. Feature extraction & image processing, second edition, 2nd ed., Academic Press.

Worsley, K. J. 1994. Local maxima and the expected Euler characteristic of excursion sets of χ^2, F and t fields, Advances in Applied Probability 26, 13–42.

Worsley, K. J. 2007. Random field theory. In: Statistical parametric mapping: the analysis of functional brain images (K.J. et al. Friston, ed.), Elsevier/Academic Press, Amsterdam.

Worsley, K. J., Andermann, M., Koulis, T., Macdonald, D., and Evans, A. C. 1999. Detecting changes in nonisotropic images, Human Brain Mapping 8, 98–101.

Worsley, K. J., Marrett, S., Neelin, P., Vandal, A. C., Friston, K. J., and Evans, A. C. 1996. A unified statistical approach for determining significant signals in images of cerebral activation, Human Brain Mapping 4, 58–73.